A rock-physics model to determine the pore microstructure of cracked porous rocks

Lin Zhang[1,2], Jing Ba[1] and José M. Carcione[3]

1. School of Earth Sciences and Engineering, Hohai University, Nanjing, China.

2. Earth, Atmospheric, and Planetary Sciences Department, Purdue University, West Lafayette, IN, USA.

3. National Institute of Oceanography and Applied Geophysics (OGS), Italy.

SUMMARY

Determining rock microstructure remains challenging, since a proper rock-physics model is needed to establish the relation between pore microstructure and elastic and transport properties. We present a model to estimate pore microstructure based on porosity, ultrasonic velocities and permeability, assuming that the microstructure consists on randomly oriented stiff equant pores and penny-shaped cracks. The stiff pore and crack porosity varying with differential pressure is estimated from the measured total porosity on the basis of a dual porosity model. The aspect ratio of pores and cracks and the crack density as a function of differential pressure are obtained from dry-rock P- and S-wave velocities, by using a differential effective medium (DEM) model. These results are used to invert the pore radius from the matrix permeability by using a circular pore model. Above a crack density of 0.13, the crack radius can be estimated from permeability, and below that threshold, the radius is estimated from P-wave velocities, taking into account the wave dispersion induced by local fluid flow between pores and cracks. The approach

is applied to experimental data for dry and saturated Fontainebleau sandstone and Chelmsford Granite.

Keywords: Microstructures; Permeability and porosity; Acoustic properties; Fracture and flow

1 INTRODUCTION

It is generally accepted that the physical properties of rocks are closely related to pore microstructure (Walsh, 1965). A precise characterization of the pore microstructure is critical to evaluate oil and gas reservoirs (Tang et al., 2012) and define the Earth structure (Rempe et al., 2018). To this purpose, direct microstructural observations were developed, including scanning electron microscopy (Pittman, 1971), micro X-ray CT (Spanne et al., 1994), focused ion-beam scanning electron microscopy (Curtis M E, 2012) and confocal laser microscopy (Fredrich et al., 1995). These studies indicate that the pore microstructure affects the elastic, electrical, transport and thermal properties of rocks (e.g., Zhan et al., 2010; Brantut et al., 2018; Sarout et al., 2017). Although these approaches can provide information about the microstructure, their accuracy is constrained by the resolution of the imaging techniques (Zhang and Toksöz, 2012).

To address this problem, it is essential to consider conventional experiments to characterize the pore microstructure, i.e., the establishment of relationships between the physical properties and pore microstructure. Rock-physics models consider the relation between pore microstructure and porosity (Shapiro, 2003), elastic properties (Walsh, 1965; Benveniste, 1987; Le Ravalec and Guéguen, 1996; Fortin et al., 2007), electrical properties (Garnett, 1904, 1906; Seleznev et al., 2006), transport properties (Reiss 1980;

Al-Wardy and Zimmerman, 2004; Guéguen & Schubnel, 2003) and thermal conductivity (Pimienta et al., 2014). Moreover, many other approaches have been proposed to obtain the pore microstructure from elastic properties (Cheng and Toksöz, 1979; Pervukhina et al., 2010; David et al., 2012; Zhang et al., 2019; Cheng et al., 2020), electrical properties (Han, 2018b), elastic and electrical properties (Han et al., 2016a, 2018a), and elastic and transport properties (Sarout et al., 2017; Pimienta et al., 2017). The results show that these physical properties are to some extent related (Carcione et al., 2007; Han et al., 2016b, 2018a).

While these studies mainly focus on non-porous microcracked rocks or high porosity rocks, where the microstructure is relatively simple, their results show that the contribution of pore microstructure to physical properties can be attributed to a distribution of pores or cracks (Sarout et al., 2017; Pimienta et al., 2017; Brantut et al., 2018). However, the pore microstructure is usually characterized in terms of characteristics size, geometry and connectivity of stiff pores and cracks (Zhang et al., 2019). Therefore, the characterization remains challenging due to the complexity of the pore space and there is not a clear relationship between microstructure and physical properties.

In this work, we propose a new combination of models to characterize the pore microstructure. We consider two rocks showing a similar dependency on pressure, namely Fontainebleau sandstone (Pimienta et al., 2015a, 2015b) and Chelmsford Granite (Coyner, 1984) and assume that the pore microstructure consists of randomly oriented stiff pores and cracks (Figure 1). Then, we adopt the model developed by Zhang et al. (2019).

2 THEORETICAL MODELS

In the following sections, we discuss the relations between porosity, elastic properties, permeability and pore microstructure. An effective model is used to characterize the pore microstructure (Figure 2).

2.1. Porosity and pore microstructure

As reported in the literature (e.g., Shapiro, 2003; Pervukhina et al., 2010; Ji et al., 2012), Shapiro (2003) assumed that variations in stiff pore porosity are independent of crack porosity and that the compressibility of the dry-rock skeleton as a function of porosity is linear. The pore-space microstructure can be represented by a dual porosity model (equant pores and cracks). Total porosity ϕ is the sum of stiff pore (ϕ_p) and crack porosity (ϕ_c),

$$\phi(P_d)=\phi_p(P_d)+\phi_c(P_d), \tag{1}$$

with

$$\phi_p(P_d)=\phi_{p0}-P_d\left(C_{drs}-C_{gr}\right), \tag{2}$$

$$\phi_c(P_d)=\phi_{c0}\exp\left(-\theta_c C_{drs} P_d\right), \tag{3}$$

where ϕ_{p0} and ϕ_{c0} are the pore and crack porosities at zero pressure, respectively, $C_{drs}=1/K_{drs}$, where K_{drs} is the dry-rock bulk modulus with all the cracks closed, $C_{gr}=1/K_{gr}$, where K_{gr} is the grain bulk modulus, θ_c is a pressure sensitivity coefficient related to the shape of the cracks, and P_d is the differential pressure (confining minus pore ones). Because the cracks are assumed to be closed at high differential

pressures, ϕ_p can be obtained from a linear fit of the total porosity in that range. Then, ϕ_c is estimated by subtracting the stiff porosity from the total porosity, and it is approximated by an exponential function (Shapiro, 2003; Liu et al., 2009).

2.2. Dry-rock properties and pore microstructure

A multistep methodology is proposed to model the elastic properties (e.g., Fortin et al., 2007; David et al., 2012), where cracks are introduced into a host material containing the stiff pores. First, the differential effective medium theory (Benveniste, 1987) is applied to model the effective moduli (K_p, G_p) of the dry rock containing randomly oriented stiff pores, represented by spheroidal inclusions. We have

$$\left(1-\phi_p\right)\frac{1}{K_p}\frac{\mathrm{d}K_p}{\mathrm{d}\phi_p}=-P, \tag{4}$$

$$\left(1-\phi_p\right)\frac{1}{G_p}\frac{\mathrm{d}G_p}{\mathrm{d}\phi_p}=-Q, \tag{5}$$

with the initial conditions $K_p\left(\phi=0\right)=K_{gr}$ and $G_p\left(\phi=0\right)=G_{gr}$, where G_{gr} is the grain shear modulus, P and Q are the normalized compressibility and shear compliances of the pores, whose expressions can be found in Appendix A (David and Zimmerman, 2011). For dry pores, P and Q are functions of the spheroidal aspect ratio α and Poisson's ratio of the grains ν_{gr}. Hence, the aspect ratio of the stiff pores (α) can be obtained from the elastic moduli at high pressure (cracks closed).

Following Walsh (1965) and David and Zimmerman (2012), it can be assumed that cracks are penny shaped, and have the same radius R_0 and height h, with aspect ratio $\gamma=h/\left(2R_0\right)$ (Figure 1). Then, the penny shaped cracks are introduced into the host

material composed of minerals and stiff pores. The relation between crack density (ε) and elastic moduli (K, ν) are established by using a differential effective medium theory (Benveniste, 1987) as

$$\frac{K}{K_p} = \frac{\left(1-2v_p\right)e^{-16\varepsilon/9}}{1-2v_p e^{-8\varepsilon/5}}, \tag{6}$$

$$\frac{v}{v_p} = e^{-8\varepsilon/5}, \tag{7}$$

where $v_p = \left(3K_p - 2G_p\right)/\left(6K_p + 2G_p\right)$ is the Poisson ratio of the host material. Hence, the crack density ε can be obtained from the pressure-dependent elastic moduli. In addition, by using the crack porosity estimated in Section 2.1, the crack aspect ratio γ is calculated by the relation $\phi_c = \left(4/3\right)\pi\varepsilon\gamma$ (e.g., Thomsen, 1995; David and Zimmerman, 2012).

2.3. Permeability and pore microstructure

The total permeability contributed by pores and cracks can be expressed as (Bernabe, 1991; Shapiro et al., 2015; Zheng et al., 2015)

$$\kappa\left(P_d\right) = \kappa_p\left(P_d\right) + \kappa_c\left(P_d\right), \tag{8}$$

where κ_p is the matrix permeability related to the spheroidal pores and κ_c is the crack permeability. Equation (8) assumes that fluids move through the medium through two parallel pore systems. Similar to the porosity, κ_p can be obtained at high pressures, approximated by a linear function (Shapiro et al., 2015) or an exponential function (Zheng et al., 2015), while κ_c is estimated by subtracting the matrix permeability from

the total permeability and can be approximated by an exponential fit (Zheng et al., 2015). Both the linear and exponential fits are convenient mathematical forms to empirically describe the pressure dependent behavior.

To investigate the relation between permeability and pore microstructure, several effective models have been developed (Guéguen & Schubnel, 2003; Zhang et al., 2016). If we consider a rock with circular tubes of pore radius r, the matrix permeability is (Al-Wardy and Zimmerman, 2004)

$$\kappa_p = \frac{\phi_p r^2}{8}. \tag{9}$$

If we assume a rock containing only randomly-oriented penny-shaped cracks and crack aspect ratio is very low at each differential pressure, i.e. $\gamma_i \ll 1$, the permeability is (Sarout, 2012)

$$\kappa_c \sim \frac{4}{27}\phi_c R_i^2 \gamma_i^2, \tag{10}$$

where R_i is the crack radius at each differential pressure. In this case, there is percolation threshold at a crack density of $\varepsilon_{percolation}$ ~0.13 (e.g., Sarout et al., 2017). Above this value, the crack and pore radius can be estimated from the measured permeability.

2.4. Saturated-rock elastic properties and pore microstructure

The cracks, when the crack density is less than 0.13, only affect the elastic properties and not the permeability, and their radii can be estimated from the saturated-rock elastic properties. These are given by wave propagation equations for cracked porous media (see Appendix B), which describe the wave dispersion characteristics induced by the local fluid flow related to the microstructure (Zhang et al., 2019). By substituting a plane-wave

kernel into the equations, we can obtain the Christoffel equation:

$$\begin{vmatrix} a_{11}k^2+b_{11} & a_{12}k^2+b_{12} & a_{13}k^2+b_{13} \\ a_{21}k^2+b_{21} & a_{22}k^2+b_{22} & a_{23}k^2+b_{23} \\ a_{31}k^2+b_{31} & a_{32}k^2+b_{32} & a_{33}k^2+b_{33} \end{vmatrix} = 0, \tag{11}$$

where

$$a_{11} = \lambda_c + \frac{2}{3}G + \phi_1\phi_2\left(\alpha_1 M_1 - \alpha_2 M_2\right)q_1, \quad b_{11} = -\rho\omega^2,$$

$$a_{12} = -\alpha_1 M_1 + \phi_1\phi_2\left(\alpha_1 M_1 - \alpha_2 M_2\right)q_2, \quad b_{12} = \rho_f\omega^2,$$

$$a_{13} = -\alpha_2 M_2 + \phi_1\phi_2\left(\alpha_1 M_1 - \alpha_2 M_2\right)q_3, \quad b_{13} = \rho_f\omega^2,$$

$$a_{21} = -\alpha_1 M_1 - \phi_1\phi_2 M_1 q_1, \quad b_{21} = b_{12},$$

$$a_{22} = M_1 - \phi_1\phi_2 M_1 q_2, \quad b_{22} = -m_1\omega^2 + i\omega b_1/\phi_1^2,$$

$$a_{23} = -\phi_1\phi_2 M_1 q_3, \quad b_{23} = 0,$$

$$a_{31} = -\alpha_2 M_2 - \phi_1\phi_2 M_2 q_1, \quad b_{31} = b_{13},$$

$$a_{32} = \phi_1\phi_2 M_2 q_2, \quad b_{32} = 0,$$

$$a_{33} = M_2 + \phi_1\phi_2 M_2 q_3,$$

with

$$q_1 = \phi_1\phi_2\left(\alpha_1 M_1 - \alpha_2 M_2\right)/Z, \quad q_2 = -\phi_1\phi_2 M_1/Z, \quad q_3 = -\phi_1\phi_2 M_2/Z,$$

$$Z = -\omega^2\left(\frac{3}{8} + \frac{\phi_{20}}{2\phi_{10}}\ln\frac{R_0+L}{R_o}\right)\phi_1^2\phi_2\rho_f R_0^2 + i\omega\left(\frac{3\eta_2}{8\kappa_2} + \frac{\eta_1}{2\kappa_1}\ln\frac{R_0+L}{R_o}\right)\phi_{20}\phi_2\phi_1^2 R_0^2 - \phi_1^2\phi_2^2\left(M_1+M_2\right),$$

where $\phi=\phi_1+\phi_2$ is the total porosity, with $\phi_1=\phi_p$ and $\phi_2=\phi_c$ are the porosities of the host medium and inclusions, respectively, $\phi_m = v_m\phi_{m0}$, where v_m and ϕ_{m0} are the volume fraction of the m phase and the matrix porosity of a local area internal to the m

phase, η is the fluid viscosity, $\kappa_1=\kappa_p$ and $\kappa_2=\kappa_c$ are the permeabilities of the host medium and inclusions, respectively, and ρ and ρ_f are the densities of the porous rock and pore fluid, where $\rho=(1-\phi)\rho_{gr}+\phi\rho_f$, with ρ_{gr} the grain density. The coefficients m_1 and m_2 are given by $m_1=\tau_1\rho_f/\phi_1$ and $m_2=\tau_2\rho_f/\phi_2$ (Biot, 1962), with τ_1 and τ_2 representing the tortuosities of the host medium and inclusions, respectively. Moreover, G is the dry-rock shear modulus and λ_c, α_1, α_2, M_1, M_2 are stiffness coefficients, whose expressions can be found in Appendix C (Zhang et al., 2019). The fluid variation by fluid flow between the host medium and inclusions is denoted by ς, and $L=\left(R_0^2/12\right)^{1/2}$ is the characteristic flow length.

The wavenumber k, solution of equation (11), is used to obtain the P-wave phase velocity of the saturated rock as $v_P=\left(\mathrm{Re}\left(k/\omega\right)\right)^{-1}$, where ω is the angular frequency. Finally, the crack radius can be estimated from the measured P-wave velocities.

3 RESULTS

Two rock samples are selected, namely, Fontainebleau sandstone and Chelmsford granite, whose rock properties at normal conditions are given in Table 1. The two samples are measured at a frequency of 0.5 and 1 MHz, and at a range of differential pressure from 1 to 50 and from 0 to 100 MPa, respectively. A detailed description of the sample characterization and measurement procedure can be found in Pimienta et al. (2015a, 2015b), Nadan and Engelder (2009) and Coyner (1984).

3.1. Estimation of pore and crack porosity

The pressure dependency of the stiff pores and crack porosity, by fitting the experimental porosity with the dual-porosity model, is shown in Figure 3, where the goodness of fit (R^2) is 0.999 for two samples. For Fontainebleau sandstone, $\phi_p = 6.952 - 0.003357 * P_d$ (%) and $\phi_c = 0.06474 * \exp(-0.2276 * P_d)$ (%), where P_d is given in MPa. For Chelmsford granite, $\phi_p = 0.8556 - 0.001134 * P_d$ (%) and $\phi_c = 0.2501 * \exp(-0.07217 * P_d)$ (%). These results show that the fraction of cracks of Fontainebleau sandstone is less than that of Chelmsford granite.

3.2. Estimation of the pore and crack aspect ratios

The P- and S-wave velocities as a function of differential pressure for dry Fontainebleau sandstone and Chelmsford granite are shown in Figure 4, used to estimate the pore and crack aspect ratios. As discussed in Section 2.2, the dry-rock bulk and shear moduli are first estimated from the measured P- and S-wave velocities at high pressures. The inferred aspect ratios of the stiff pores are 0.18 (the error on the P- and S-wave velocities is 0.67 % for Fontainebleau sandstone) and 0.03 (the error is 1 % for Chelmsford granite). The crack density and aspect ratio for the two samples at each differential pressure are shown in Figure 5. The crack density decreases monotonically with increasing differential pressure, indicating that the cracks close gradually with increasing pressure. The contribution of the cracks to the permeability vanishes when the crack density is less than 0.13, whereas the effect of these cracks on the elastic properties is relevant. Similar conclusions were obtained for high porosity rocks, but the contribution of the cracks to the transport properties was not considered (Pimienta et al., 2017).

The evolution of the crack aspect ratio with differential pressure is estimated by using the inferred crack porosity and density. Compared to the crack density, the evolution of the crack aspect ratio is non-monotonic for Fontainebleau sandstone, which is similar to the results reported by Sarout et al. (2017), whereas the trend is monotonic for Chelmsford granite. Note that our procedure differs markedly from that of David and Zimmermann (2012) who instead use the pressure dependence of the crack density and the physics of pressure-induced crack closure to infer, more realistically, a distribution of zero-pressure crack aspect ratios. In this work, the crack density inferred from the modulus deficits is related to the crack porosity estimated at the same pressure through eqs. (1-3), by an effective aspect ratio. Thus, a model crack microstructure is established that involves open cracks with a common, pressure-dependent, aspect ratio. In addition, based on the relation $P_c \sim E\gamma$, the aspect ratios for crack closure are also given in Figure 5. The aspect ratios for crack closure increase with increasing differential pressure, implying that the cracks with lower aspect ratio close first under increasing differential pressure. The effective aspect ratios of the open cracks decrease with increasing differential pressure, implying that the cracks generally become flat under increasing differential pressure.

3.3. Estimation of pore and crack radii

Figure 6 shows the comparison between the experimental and predicted permeabilities, based on equations (8) to (10), where Fontainebleau sandstone is saturated with water and Chelmsford granite with nitrogen. Similar to the discussion on porosity, the total permeability can be divided into the matrix and crack permeabilities, which can be approximated by exponential functions (Zheng et al., 2019), with R^2=0.998 for

Fontainebleau sandstone and R^2=0.999 for Chelmsford granite. We obtain $\kappa_p = 2.004 * \exp(-0.001837 * P_d)$ and $\kappa_p = 1.54 * \exp(-0.04279 * P_d)$, and $\kappa_c = 2.765 * \exp(-0.3632 * P_d)$ and $\kappa_c = 31.42 * \exp(-0.3225 * P_d)$, respectively. Note that the crack permeability cannot be neglected in comparison with the matrix permeability at low differential pressures. The former is greater than the matrix permeability for Chelmsford granite, which is consistent with the result of Zheng et al. (2019), but this is different for high porosity rocks (Pimienta et al., 2017).

As discussed in Sections 3.1 and 3.2, the porosity and aspect ratios of pores and cracks are estimated from the known porosity and dry-rock velocities. These are used as input for the effective permeability model to predict the pressure dependency of pores and crack radii. Hence, the best fit between the modeled and measured data provides the range of pore radius at all differential pressures, while in comparison with $\varepsilon_{percolation}$ ~0.13, the contribution of cracks to the total permeability are mostly distributed in the range of 1~5 MPa (Fontainebleau sandstone) and 0~30 MPa (Chelmsford granite). The range of the crack radius is estimated at low differential pressures. To estimate the whole range, the pressure dependency of the saturated-rock velocities is modeled with equation (11). Note that all the input parameters (i.e., porosity, aspect ratio and radii of pores and cracks) are estimated at low differential pressures. The tortuosities of the host medium and inclusions are $\tau_m = 1/2\left(1 + 1/\phi_{m0}\right)$ (Berryman, 1979), the crack bulk modulus is $K_{b2} = K_c = (\pi/2)\gamma G_p / \left(1 - \nu_p\right)$ (Zatsepin and Crampin 1997), and the dry-rock modulus of the host medium is that at high differential pressure, i.e. K_{b1}=32.1 GPa (Fontainebleau sandstone) and 44.9 GPa (Chelmsford granite). Moreover, ϕ_{20} = 0.30

from a fit of the P-wave velocities of saturated rocks at low differential pressures (this value is in agreement with that of Pride et al. (2004)). It is assumed that ϕ_{20} is constant as the differential pressure changes. These are used as input properties in equation (11) (those at normal conditions are listed in Table 1), to estimate the crack radius at high differential pressures. The P-wave velocities are measured at ultrasonic frequencies and wave dispersion induced by local fluid flow affects the estimated crack radius. Then, we consider the P-wave velocities at low frequencies, where the pore fluid has enough time to equilibrate. The dry-rock moduli at low and high frequencies are very similar (e.g., Sarout et al., 2017; Schijns et al., 2018), and the saturated-rock velocities at low frequencies can be calculated with Gassmann equation. Finally, the crack radius is estimated from the P-wave velocities of the saturated rock at low and high frequencies.

The comparison of the theoretical and experimental P-wave velocities for the two samples are shown in Figure 7. The pore fluids are water for Fontainebleau sandstone (K_f =2.25 GPa, ρ_f = 1000 kg/m^3, η=0.00089 Pa•s) and benzene for Chelmsford granite (K_f =1.21 GPa, ρ_f = 880 kg/m^3, η=0.000652 Pa•s). Due to the small range of differential pressures, the effect of pressure on the fluid properties can be ignored. To account for the measured P-wave velocities, we also report the results from Gassmann equation (Gassmann, 1951), the squirt-flow model (Gurevich et al., 2010) and equation (11). It appears that equation (11) is in better agreement with Gassmann equation at low frequencies, but this equation fails to explain the measurements. The predictions from the squirt-flow model and equation (11) are better, since these models consider the local fluid flow between pores and cracks. The differences between predictions and measurements can be attributed to the fact that at low differential pressures, there other dispersion

mechanisms induced by the cracks, such as scattering. Moreover, we assume idealized penny-shaped cracks. These differences gradually decrease with increasing differential pressure due to the closure of cracks. Similar conclusions can be found in previous works (e.g., Adelinet et al., 2010; Li et al., 2018).

The pressure dependency of the pore and crack radii is given in Figures 8 and 9, respectively. It is shown that there is no variation of pore radius for Fontainebleau sandstone, compared to a decrease of pore radius for Chelmsford granite as differential pressure increases. The nearly pressure independency for Fontainebleau sandstone may be due to the fact that κ_p and ϕ_p do not depend on pressure, which means that the grains are well sorted, as reported by Pimienta et al. (2015a). The crack radius decreases with increasing differential pressure for the two samples. Note also that the range of crack radius is larger than that of pore radius, which indicates that the pressure sensitivity to cracks is higher.

4 DISCUSSION

4.1. Assessment of model assumption

To model the pressure dependency of the rock properties, the assumption is that the pore space is described by pores (insensitive to pressure) and cracks (sensitive to pressure). The modeling results suggest that this assumption is enough to explain the pressure-dependent physical properties, and use the present approach to characterize the pore microstructure. In addition, the assumption is also confirmed by the microscopic image of Fontainebleau sandstone, which can be found in Pimienta et al. (2015a). The

pore structure of rocks is composed of a distribution of stiff (equant) pores and cracks. However, this decomposition is not unique and, for instance, Sun et al. (2018) divide the pore structure into three parts: stiff pores, compliant pores (cracks) and intermediate pores. Hence, the estimated crack porosity is uncertain, since it depends on the decomposition of the pore structure and the pressure range.

4.2. Assessment of the estimated crack density

To estimate the crack density, the differential effective medium (DEM) model allows us to analyze the interaction between cracks and pores, and avoids overestimated crack densities by using the non-interaction approximation (Pimienta et al., 2018). To highlight the interaction between cracks, a comparison between the DEM and Mori-Tanaka (MT) models (Benveniste, 1987) for predicting crack density is shown in Figure 10. The MT model accounts for interactions between the pores, but the interaction between cracks is neglected. For Fontainebleau sandstone, when the crack density is less than 0.1, the two models predict the same crack density, while they give different results as crack porosity increases (corresponding to decreasing differential pressure). These conclusions are consistent with the results of Pimienta et al (2018), implying that the MT model overestimates the crack density compared to the DEM model at low differential pressures. A similar behavior can be observed for Chelmsford granite at low differential pressures, whereas the predicted crack density from the DEM model is slightly higher than that of the MT model as the crack porosity decreases, which suggest that the DEM model can fully account for the presence of cracks and it is suitable to estimate the crack distribution.

4.3. Assessment of the estimated cracks radius

A major concern about permeability is that the measurements depend on the type of fluid nature (nitrogen and benzene in this case), and further work is needed to measure the physical properties at the same experimental conditions. In addition, as described in Section 3, the results indicate that cracks are dominant at low differential pressures, corresponding to crack densities above 0.13, and although cracks close with increasing differential pressure, their effect cannot be neglected. To estimate the crack radius, the assumption that the total permeability is the sum of matrix and crack permeabilities has been proposed. However, cracks and pores may be interconnected in a complex pattern instead of following a parallel connection, and therefore more work is required to develop a proper effective permeability model.

To estimate the crack radius, the dry-rock modulus of the host medium K_{b1} and the matrix porosity of cracks ϕ_{20}, are required in equation (11). Considering that the stiff pores are insensitive to pressure, K_{b1} can be approximated by the value at high differential pressures, and ϕ_{20} is estimated to be 0.3 % from P-wave velocities of at low differential pressures. This value of ϕ_{20} may be different for different rocks or different pressure conditions. For the sake of simplicity, the two parameters are assumed to be constant at all differential pressures, so that the crack radius at high differential pressures can be predicted from P-wave velocities of saturated rocks at low and high frequencies.

4.4 Comparison with previous models

Our model is built on the basis of the observed pressure dependence of the porosity and

of the elastic properties of the dry and saturated medium, with additional simple expressions of the permeabilities of pores and cracks. A potentially significant over-simplification, relative to the approach of David and Zimmermann (2012), is the assumption of a single effective crack aspect ratio at any given pressure rather than a distribution of cracks. However the "effective" value provides an approach to describe the effect of cracks on permeability. This is not the case in David and Zimmermann (2012) and Li et al (2018), because they predicted saturated-rock velocities using effective medium theories, where the effect of permeability and local fluid flow between pores and cracks are not considered. Though Gurevich et al. (2010) analyzed the effect of local fluid flow, the effect of permeability is also not included.

5 CONCLUSIONS

We propose a model to characterize the aspect ratio and radii of pores and cracks from the experimental porosity, elastic properties and permeability as a function of the differential pressure. The results show that a complete characterization is achieved compared with the previous models, and a significant variation of the rock physical properties is mainly due to the crack behavior at low differential pressures. Further studies should be performed to compare these characteristics with the actual microstructural observations. Our model does not explain the experimentally observed stiffening of the medium by fluid saturation, which implies that a distribution of pores and cracks should be considered, and in such fluid-saturated media, it has been suggested that the waves might selectively follow fast paths that avoid much of the porosity. Moreover, our model can be extended to predict other physical properties, such as

electrical resistivity and thermal conductivity.

ACKNOWLEDGEMENTS

We thank I. Jackson and one anonymous reviewers for their valuable comments and suggestions, and we are also very grateful to two editors for suggestions. We thank Lucas Pimienta for providing the experimental data of Fontainebleau sandstone and Douglas Schmitt for comments to improve the paper. This work is supported by the Cultivation Program of '111' Project of China, Distinguished Professor Program of Jiangsu Province, China, the National Natural Science Foundation of China (No. 41704109, 41974123) and the Fundamental Research Funds for the Central Universities (B200203010).

REFERENCES

Adelinet, M., Fortin, J., Guéguen, Y., Schubnel, A., & Geoffroy, L., 2010. Frequency and fluid effects on elastic properties of basalt: Experimental investigations. *Geophys. Res. Lett.*, 37(2). https://doi.org/10.1029/2009GL041660.

Adelinet, M., Fortin, J., & Guéguen, Y., 2011. Dispersion of elastic moduli in a porous-cracked rock: Theoretical predictions for squirt-flow. *Tectonophysics, 503*(1-2), 173-181. https://doi.org/10.1016/j.tecto.2010.10.012.

Al-Wardy, W., & Zimmerman, R. W., 2004. Effective stress law for the permeability of clay-rich sandstones. *J. Geophys. Re.s: Solid. Earth., 109*(B4). https://doi.org/10.1029/2003JB002836.

Ba, J., J. M. Carcione, and J. X. Nie., 2011. Biot-Rayleigh theory of wave propagation in double-porosity media: *J. Geophys. Res: Solid. Earth., 116*, B06202. https://doi:

10.1029/2010JB008185.

Benveniste, Y., 1987. A new approach to the application of Mori-Tanaka's theory in composite materials. *Mechanics of materials,* *6*(2), 147-157. doi: 10.1016/0167-6636(87)90005-6.

Bernabe, Y., 1991. Pore geometry and pressure dependence of the transport properties in sandstones. *Geophysics*, *56*(4), 436-446. https://doi.org/10.1190/1.1443061.

Berryman, J. G., 1979. Theory of elastic properties of composite materials. *Appl. Phys. Lett., 35*(11), 856-858. https://doi.org/10.1063/1.90982.

Biot, M. A., 1962. Mechanics of deformation and acoustic propagation in porous media. *J. Appl. Phys., 33*(4), 1482-1498. https://doi.org/10.1063/1.1728759.

Brantut, N., Baker, M., Hansen, L. N., & Baud, P., 2018. Microstructural control of physical properties during deformation of porous limestone. *J. Geophy.s Res: Solid. Earth., 123*(6), 4751-4764. https://doi.org/10.1029/2018JB015636.

Carcione, J. M., Ursin, B., & Nordskag, J. I., 2007. Cross-property relations between electrical conductivity and the seismic velocity of rocks. *Geophysics, 72*(5), E193-E204. http://dx.doi.org/10.1190/1.2762224.

Coyner, K. B., 1984. Effects of stress, pore pressure, and pore fluids on bulk strain, velocity, and permeability in rocks (Doctoral dissertation, Massachusetts Institute of Technology).

Cheng, C. H., & Toksöz, M. N., 1979. Inversion of seismic velocities for the pore aspect ratio spectrum of a rock. *J. Geophys. Res: Solid. Earth., 84*(B13), 7533-7543. https://doi.org/10.1029/JB084iB13p07533.

Cheng, W., Carcione, J. M., Qadrouh, A. N., Alajmi, M., and Ba, J., 2020. Rock

anelasticity, pore geometry and the Biot-Gardner effect, *Rock Mechanics and Rock Engineering*, in press.

Curtis, M. E., Sondergeld, C. H., Ambrose, R. J., & Rai, C. S., 2012. Microstructural investigation of gas shales in two and three dimensions using nanometer-scale resolution imaging. *AAPG bulletin, 96*(4), 665-677. https://doi.org/10.1306/08151110188.

David, E. C., & Zimmerman, R. W., 2011. Compressibility and shear compliance of spheroidal pores: Exact derivation via the Eshelby tensor, and asymptotic expressions in limiting cases. *Int. J. Solids. Struct., 48*(5), 680-686. https://doi.org/10.1016/j.ijsolstr.2010.11.001.

David, E. C., & Zimmerman, R. W., 2012. Pore structure model for elastic wave velocities in fluid-saturated sandstones. *J. Geophys. Res: Solid. Earth., 117*(B7). https://doi.org/10.1029/2012JB009195.

de Paula, O. B., Pervukhina, M., Makarynska, D., & Gurevich, B., 2012. Modeling squirt dispersion and attenuation in fluid-saturated rocks using pressure dependency of dry ultrasonic velocities. *Geophysics, 77*(3), WA157-WA168. https://doi.org/10.1190/geo2011-0253.1.

Fortin, J., Guéguen, Y., & Schubnel, A., 2007. Effects of pore collapse and grain crushing on ultrasonic velocities and Vp/Vs. *J. Geophys. Res: Solid. Earth., 112*(B8). https://doi.org/10.1029/2005JB004005

Fredrich, J. T., Menendez, B., & Wong, T. F., 1995. Imaging the pore structure of geomaterials. *Science, 268*(5208), 276-279. doi: 10.1126/science.268.5208.276.

Garnett, J. M., 1904. XII. Colours in metal glasses and in metallic films. *Philosophical*

Transactions of the Royal Society of London. Series A, Containing Papers of a Mathematical or Physical Character, 203(359-371), 385-420. https://doi.org/10.1098/rsta.1904.0024.

Garnett, J. M., 1906. VII. Colours in metal glasses, in metallic films, and in metallic solutions.—II. *Philosophical Transactions of the Royal Society of London. Series A, Containing Papers of a Mathematical or Physical Character, 205*(387-401), 237-288. https://doi.org/10.1098/rsta.1906.0007.

Gassmann, F., 1951. Über die Elastizität poröser Medien: Vierteljahrsschrift der Naturforschenden Gesellschaft in Zürich, 96, 1–23.

Guéguen, Y., & Schubnel, A., 2003. Elastic wave velocities and permeability of cracked rocks. *Tectonophysics, 370*(1–4), 163–176. https://doi.org/10.1016/s0040-1951(03)00184-7.

Gurevich, B., Makarynska, D., de Paula, O. B., & Pervukhina, M., 2010. A simple model for squirt-flow dispersion and attenuation in fluid-saturated granular rocks. *Geophysics, 75*(6), N109-N120. https://doi.org/10.1190/1.3509782.

Han, T., Gurevich, B., Pervukhina, M., Clennell, M. B., & Zhang, J., 2016a. Linking the pressure dependency of elastic and electrical properties of porous rocks by a dual porosity model. *Mon Not R Astron Soc, 205(*1), 378-388. https://doi.org/10.1093/gji/ggw019.

Han, T., Clennell, M. B., Cheng, A. C., & Pervukhina, M., 2016b. Are self-consistent models capable of jointly modeling elastic velocity and electrical conductivity of reservoir sandstones*?*. *Geophysics, 81*(4), D377-D382. https://doi.org/10.1190/geo2015-0690.1.

Han, T., 2018a. Joint elastic-electrical properties of artificial porous sandstone with aligned fractures. *Geophys. Res. Lett., 45*, 3051–3058. https://doi.org/10.1002/2018GL077541.

Han, T., 2018b. An effective medium approach to modelling the pressure-dependent electrical properties of porous rocks. *Geophys. J. Int.*, 214(1), 70-78. https://doi.org/10.1093/gji/ggy125.

Han, T., Liu, B., & Sun, J., 2018c. Validating the theoretical model for squirt-flow attenuation in fluid saturated porous rocks based on the dual porosity concept. *Geophys. J. Int., 214*(3), 1800-1807. https://doi.org/10.1093/gji/ggy241.

Ji, Y., Baud, P., Vajdova, V., & Wong, T. F., 2012. Characterization of pore geometry of Indiana limestone in relation to mechanical compaction. *Oil. Gas. Sci. Technol., 67*(5), 753-775. https://doi.org/10.2516/ogst/2012051.

Li, Y., David, E. C., Nakagawa, S., Kneafsey, T. J., Schmitt, D. R., & Jackson, I., 2018. A broadband laboratory study of the seismic properties of cracked and fluid - saturated synthetic glass media. *J. Geophys. Res: Solid Earth.,* 123(5), 3501-3538.

Liu, H. H., Rutqvist, J., & Berryman, J. G., 2009. On the relationship between stress and elastic strain for porous and fractured rock. *Int. J. Rock. Mech. Min. Sci., 46*(2), 289-296. https://doi.org/10.1016/j.ijrmms.2008.04.005.

Le Ravalec, M., & Guéguen, Y., 1996. High-and low-frequency elastic moduli for a saturated porous/cracked rock-differential self-consistent and poroelastic theories. *Geophysics, 61*(4), 1080-1094. https://doi.org/10.1190/1.1444029.

Markov, M., Kazatchenko, E., Mousatov, A., & Pervago, E., 2012. The dielectric permittivity of carbonate formations from the unified microstructure model. *J. Appl.*

Geophys., 76, 56-63. https://doi.org/10.1016/j.jappgeo.2011.10.006.

Mavko, G., Mukerji, T., and Dvorkin, J., 2009. The Rock Physics Handbook. Cambridge University Press, Cambridge.

Nadan, B. J., & Engelder, T., 2009. Microcracks in New England granitoids: A record of thermoelastic relaxation during exhumation of intracontinental crust. *Geol. Soc. Am. Bull., 121*(1-2), 80-99. https://doi.org/10.1130/B26202.1.

Pervukhina, M., Gurevich, B., Dewhurst, D. N., & Siggins, A. F., 2010. Applicability of velocity—stress relationships based on the dual porosity concept to isotropic porous rocks. *Geophys. J. Int., 181*(3), 1473-1479. https://doi.org/10.1111/j.1365-246X.2010.04535.x.

Pimienta, L., Sarout, J., Esteban, L., & Piane, C. D., 2014. Prediction of rocks thermal conductivity from elastic wave velocities, mineralogy and microstructure. *Geophys. J. Int., 197*(2), 860-874. https://doi.org/10.1093/gji/ggu034.

Pimienta, L., Fortin, J., & Guéguen, Y., 2015a. Bulk modulus dispersion and attenuation in sandstones. *Geophysics, 80*(2), D111-D127. https://doi.org/10.1190/geo2014-0335.1.

Pimienta, L., Fortin, J., & Guéguen, Y., 2015b. Experimental study of Young's modulus dispersion and attenuation in fully saturated sandstones. *Geophysics, 80*(5), L57-L72. https://doi.org/10.1190/geo2014-0532.1.

Pimienta, L., Sarout, J., Esteban, L., David, C., & Clennell, M. B., 2017. Pressure-Dependent Elastic and Transport Properties of Porous and Permeable Rocks: Microstructural Control. *J. Geophys. Res: Solid. Earth., 122*(11), 8952-8968. https://doi.org/10.1002/2017JB014464.

Pimienta, L., Schubnel, A., Violay, M., Fortin, J., Guéguen, Y., & Lyon-Caen, H., 2018. Anomalous Vp/Vs ratios at seismic frequencies might evidence highly damaged rocks in subduction zones. *Geophys. Res. Lett., 45*(22), 12-210. https://doi.org/10.1029/2018GL080132

Pittman, E. D., 1971. Microporosity in carbonate rocks. *AAPG Bulletin*, *55*(10), 1873-1878.

Pride, S. R., Berryman, J. G., & Harris, J. M., 2004. Seismic attenuation due to wave-induced flow. *J. Geophys. Res: Solid. Earth., 109*(B1). https://doi.org/10.1029/2003JB002639.

Reiss, L. H., 1980. The reservoir engineering aspects of fractured formations (Vol. 3). Editions Technip.

Rempe, M., Mitchell, T. M., Renner, J., Smith, S. A. F., Bistacchi, A., & Di Toro, G., 2018. The relationship between microfracture damage and the physical properties of fault-related rocks: The Gole Larghe Fault Zone, Italian Southern Alps. *J. Geophys. Res: Solid Earth., 123*, 7661–7687. https://doi.org/10.1029/2018JB015900.

Sarout, J., 2012. Impact of pore space topology on permeability, cut-off frequencies and validity of wave propagation theories. *Geophys. J. Int., 189*(1), 481-492. https://doi.org/10.1111/j.1365-246X.2011.05329.x.

Sarout, J., Cazes, E., Delle Piane, C., Arena, A., & Esteban, L., 2017. Stress-dependent permeability and wave dispersion in tight cracked rocks: Experimental validation of simple effective medium models. *J. Geophys. Res: Solid Earth., 122*(8), 6180-6201. https://doi.org/10.1002/2017JB014147.

Schijns, H., Jackson, I., & Schmitt, D. R., 2018. Shear modulus dispersion in cracked and

fluid-saturated quartzites: Experimental observations and modeling. *J. Geophys. Res: Solid Earth., 123*(4), 2825-2840. https://doi.org/10.1002/2017JB014633.

Seleznev, N. V., Habashy, T. M., Boyd, A. J., & Hizem, M., 2006. Formation properties derived from a multi-frequency dielectric measurement. *In SPWLA 47th Annual Logging Symposium. Society of Petrophysicists and Well-Log Analysts*.

Shapiro, S. A., 2003. Elastic piezosensitivity of porous and fractured rocks. *Geophysics, 68*(2), 482-486. https://doi.org/10.1190/1.1567215.

Shapiro, S. A., Khizhniak, G. P., Plotnikov, V. V., Niemann, R., Ilyushin, P. Y., & Galkin, S. V., 2015. Permeability dependency on stiff and compliant porosities: a model and some experimental examples. *J. Geophys. and Eng., 12*(3), 376-385. https://doi.org/10.1088/1742-2132/12/3/376.

Spanne, P., Thovert, J. F., Jacquin, C. J., Lindquist, W. B., Jones, K. W., & Adler, P. M., 1994. Synchrotron computed microtomography of porous media: topology and transports. *Phys. Rev. Lett*, *73*(14), 2001. https://doi.org/10.1103/PhysRevLett.73.2001.

Sun, Y., Gurevich, B., Lebedev, M., Glubokovskikh, S., Mikhaltsevitch, V., & Guo, J., 2019. A triple porosity scheme for fluid/solid substitution: theory and experiment. *Geophys. Prospect., 67*(4), 888-899. https://doi.org/10.1111/1365-2478.12677.

Tang, X. M., Chen, X. L., & Xu, X. K., 2012. A cracked porous medium elastic wave theory and its application to interpreting acoustic data from tight formations. *Geophysics, 77(6)*, D245-D252. https:// doi: 10.1190/geo2012-0091.1.

Tang, Y. B., Li, M., Bernabé, Y., Tang, H. M., Li, X. F., Bai, X. Y., & Tao, Z. W., 2015. A new electrical formation factor model for bimodal carbonates: numerical studies

using dual-pore percolation network. *Geophys. J. Int., 201*(3), 1456-1470. https://doi.org/10.1093/gji/ggv073.

Thomsen, L., 1995. Elastic anisotropy due to aligned cracks in porous rock1. *Geophys. Prospect*., 43(6), 805-829. https://doi.org/10.1111/j.1365-2478.1995.tb00282.x

Walsh, J. B., 1965. The effect of cracks on the compressibility of rock. *J. Geophys. Res., 70*(2), 381-389. https://doi.org/10.1029/JZ070i002p00381.

Zatsepin, S. V., & Crampin, S., 1997. Modelling the compliance of crustal rock—I. Response of shear-wave splitting to differential stress. *Geophys. J. Int., 129*(3), 477-494. https://doi.org/10.1111/j.1365-246X.1997.tb04488.x.

Zhan, X., Schwartz, L. M., Toksöz, M. N., Smith, W. C., & Morgan, F. D., 2010. Pore-scale modeling of electrical and fluid transport in Berea sandstone. *Geophysics, 75*(5), F135-F142. https://doi.org/10.1190/1.3463704.

Zhang, L., Ba, J., Fu, L., Carcione, J. M., & Cao, C., 2019. Estimation of pore microstructure by using the static and dynamic moduli. *Int. J. Rock. Mech. Min. Sci., 113*, 24-30. https://doi.org/10.1016/j.ijrmms.2018.11.005.

Zhang, L., Ba, J., Carcione, J. M., & Sun, W., 2019. Modeling wave propagation in cracked porous media with penny-shaped inclusions. *Geophysics, 84*(4), 1-38. https://doi.org/10.1190/geo2018-0487.1.

Zhang, R., Ning, Z., Yang, F., Zhao, H., & Wang, Q., 2016. A laboratory study of the porosity-permeability relationships of shale and sandstone under effective stress. *Int. J. Rock. Mech. Min. Sci., 100*(81), 19-27. https://doi.org/10.1016/j.ijrmms.2015.11.006.

Zhang, Y., & Toksöz, M. N., 2012. Impact of the cracks lost in the imaging process on

computing linear elastic properties from 3D microtomographic images of Berea sandstone. *Geophysics, 77*(2), R95-R104. https://doi.org/10.1190/geo2011-0126.1.

Zheng, J., Zheng, L., Liu, H. H., & Ju, Y., 2015. Relationships between permeability, porosity and effective stress for low-permeability sedimentary rock. *Int. J. Rock. Mech. Min. Sci., 78*, 304-318. https://doi.org/10.1016/j.ijrmms.2015.04.025.

Appendix A (P and Q)

P and *Q* are the normalized compressibility and shear compliances of dry pores, which depend on the spheroidal aspect ratio, α, and Poisson's ratio of the grains, v_{gr}:

$$P=\frac{\left(1-v_{gr}\right)}{6\left(1-2v_{gr}\right)}\times\frac{4\left(1+v_{gr}\right)+2\alpha^2\left(7-2v_{gr}\right)-\left[3\left(1+4v_{gr}\right)+12\alpha^2\left(2-v_{gr}\right)\right]g}{2\alpha^2+\left(1-4\alpha^2\right)g+\left(\alpha^2-1\right)\left(1+v_{gr}\right)g^2} \tag{A1}$$

$$\begin{aligned}Q=&\frac{4\left(\alpha^2-1\right)\left(1-v_{gr}\right)}{15\left\{8\left(v_{gr}-1\right)+2\alpha^2\left(3-4v_{gr}\right)+\left[\left(7-8v_{gr}\right)-4\alpha^2\left(1-2v_{gr}\right)\right]g\right\}}\\&\times\left\{\frac{8\left(1-v_{gr}\right)+2\alpha^2\left(3+4v_{gr}\right)+\left[\left(8v_{gr}-1\right)-4\alpha^2\left(5+2v_{gr}\right)\right]g+6\left(\alpha^2-1\right)\left(1+v_{gr}\right)g^2}{2\alpha^2+\left(1-4\alpha^2\right)g+\left(\alpha^2-1\right)\left(1+v_{gr}\right)g^2}\right.\\&\left.-3\left[\frac{8\left(v_{gr}-1\right)+2\alpha^2\left(5-4v_{gr}\right)+\left[3\left(1-2v_{gr}\right)+6\alpha^2\left(v_{gr}-1\right)\right]g}{-2\alpha^2+\left[\left(2-v_{gr}\right)+\alpha^2\left(1+v_{gr}\right)\right]g}\right]\right\}\end{aligned} \tag{A2}$$

$$g=\begin{cases}\dfrac{\alpha}{\left(1-\alpha^2\right)^{3/2}}\left(\arccos\alpha-\alpha\sqrt{1-\alpha^2}\right) & (\alpha<1)\\[2ex] \dfrac{\alpha}{\left(1-\alpha^2\right)^{3/2}}\left(\alpha\sqrt{1-\alpha^2}-\operatorname{arccosh}\alpha\right) & (\alpha>1)\end{cases} \tag{A3}$$

where $v_{gr}=\left(3K_{gr}-2G_{gr}\right)/\left(6K_{gr}+2G_{gr}\right)$.

Appendix B. Wave Propagation Equations for Cracked Porous Media

Following Zhang et al. (2019), the wave propagation equations for cracked porous media can be expressed by

$$2G\nabla e_{ij} + \lambda_c \nabla e - \alpha_1 M_1 \nabla\left(\xi^{(1)} - \phi_1\phi_2\varsigma\right) - \alpha_2 M_2 \nabla\left(\xi^{(2)} + \phi_1\phi_2\varsigma\right) = \rho\ddot{u} + \rho_f \ddot{w}_i^{(1)} + \rho_f \ddot{w}_i^{(2)}, \tag{B1}$$

$$\alpha_1 M_1 \nabla e - M_1 \nabla\left(\xi^{(1)} - \phi_1\phi_2\varsigma\right) = \rho_f \ddot{u} + m_1 \ddot{w}_i^{(1)} + \frac{\eta}{\kappa_1}\frac{\phi_{10}}{\phi_1}\dot{w}_i^{(1)}, \tag{B2}$$

$$\alpha_2 M_2 \nabla e - M_2 \nabla\left(\xi^{(2)} + \phi_1\phi_2\varsigma\right) = \rho_f \ddot{u} + m_2 \ddot{w}_i^{(2)} + \frac{\eta}{\kappa_2}\frac{\phi_{20}}{\phi_2}\dot{w}_i^{(2)}, \tag{B3}$$

$$\left(\frac{3}{8} + \frac{\emptyset_{20}}{2\emptyset_{10}}\ln\frac{R_0+L}{R_0}\right)\emptyset_1^2\emptyset_2\rho_f R_0^2\ddot{\varsigma} + \left(\frac{3\eta}{8\kappa_2} + \frac{\eta}{2\kappa_1}\ln\frac{R_0+L}{R_0}\right)\emptyset_{20}\emptyset_1^2\emptyset_2 R_0^2\dot{\varsigma} =$$

$$\phi_1\phi_2(\alpha_1 M_1 - \alpha_2 M_2)e + \phi_1\phi_2\left(M_2\xi^{(2)} - M_1\xi^{(1)}\right) + \emptyset_1^2\emptyset_2^2(M_1 + M_2)\varsigma\,, \tag{B4}$$

where $e_{ij} = 1/2\left(\partial_j u_i + \partial_i u_j\right)$ are the solid strain components (where i, j=1, 2, 3 represent the coordinates), $e=\nabla\cdot\mathbf{u}$. $\xi^{(m)} = -\nabla\cdot\mathbf{w}^{(m)}$ is the increment of fluid content (m=1, 2 refer to the host medium and penny-shaped inclusions (cracks), respectively), $\mathbf{w}^{(m)} = \phi_m\left(\mathbf{U}^{(m)} - \mathbf{u}\right)$, where $\mathbf{U} = \left(U_1, U_2, U_3\right)^T$ and $\mathbf{u} = \left(u_1, u_2, u_3\right)^T$ are the fluid and solid displacements, respectively. A dot above a variable denotes a partial time derivative.

Appendix C. Expressions of the Stiffness Coefficients

Following Ba et al. (2011), the stiffness coefficients can be given by

$$\lambda_c = \left(1-\phi\right)K_{gr} - \frac{2}{3}G + \left(2 - \frac{K_{gr}}{K_f}\right)\left(\phi_1\alpha_1 M_1 + \phi_2\alpha_2 M_2\right) - \left(1 - \frac{K_{gr}}{K_f}\right)\left(\phi_1^2 M_1 + \phi_2^2 M_2\right), \tag{C1}$$

$$\alpha_1 = \frac{\beta\phi_1 K_{gr}}{\chi K_f} + \phi_1 \quad , \alpha_2 = \frac{\phi_2 K_{gr}}{\chi K_f} + \phi_2 \quad , \tag{C2}$$

$$M_1 = \frac{K_f}{(\beta/\chi + 1)\phi_1}, M_2 = \frac{K_f}{(1/\chi + 1)\phi_2}, \tag{C3}$$

$$\chi = \frac{K_{gr}}{K_f}\left(\frac{\beta\phi_1 + \phi_2}{1 - \phi - K_b/K_{gr}}\right), \tag{C4}$$

$$\beta = \frac{\phi_{20}}{\phi_{10}}\left[\frac{1-(1-\phi_{10})K_{gr}/K_{b1}}{1-(1-\phi_{20})K_{gr}/K_{b2}}\right], \tag{C5}$$

where K_b=K, the dry-rock moduli of the host medium and crack are K_{b1} and K_{b2}, respectively.

Table 1. Input properties of Fontainebleau sandstone and Chelmsford Granite at normal conditions: K_{gr}, G_{gr} and ρ_{gr} are the bulk modulus, shear modulus and density of the solid grains; K_f, ρ_f and η are those of the fluid; K and G are the bulk and shear moduli of the dry rock; ϕ_1 (ϕ_2) and κ_1 (κ_2) are the matrix porosity and permeability of the host medium (inclusions); and ε, γ and R_0 are the crack density, aspect ratio and radius.

Parameter	Fontainebleau sandstone	Chelmsford Granite
K_{gr} (GPa)	37[a]	56[b]
G_{gr} (GPa)	44[a]	35.6
ρ_{gr} (kg/m^3)	2650[a]	2625[b]
K_f (GPa)	2.2[c]	1.21[b]
ρ_f (kg/m^3)	1000[c]	880[b]
η (Pa•s)	0.001[c]	0.000652[b]
G (GPa)	9.957	15.571
K (GPa)	13.216	17.285
K_{b1} (GPa)	32.1	44.9
K_{b2} (GPa)	0.0038	0.0396
ϕ_1 (%)	6.95	0.86
ϕ_2 (%)	0.0516	0.25
κ_1 (mD)	2	31.4
κ_2 (mD)	1.92	1.54
ε	0.6243	0.4355
γ	0.000197	0.0014
R_0 (m)	0.0254	0.0067

[a] data after Mavko et al. (2009).

[b] data after Coyner (1984).

[c] data after Pimienta et al. (2015a, 2015b).

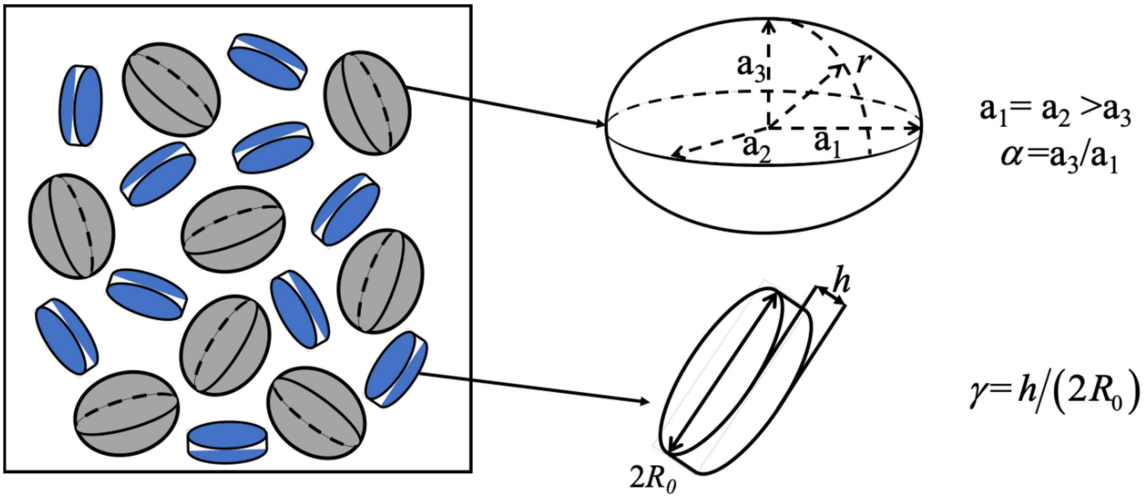

Figure 1. Conceptual model of the rock microstructure of a cracked porous medium

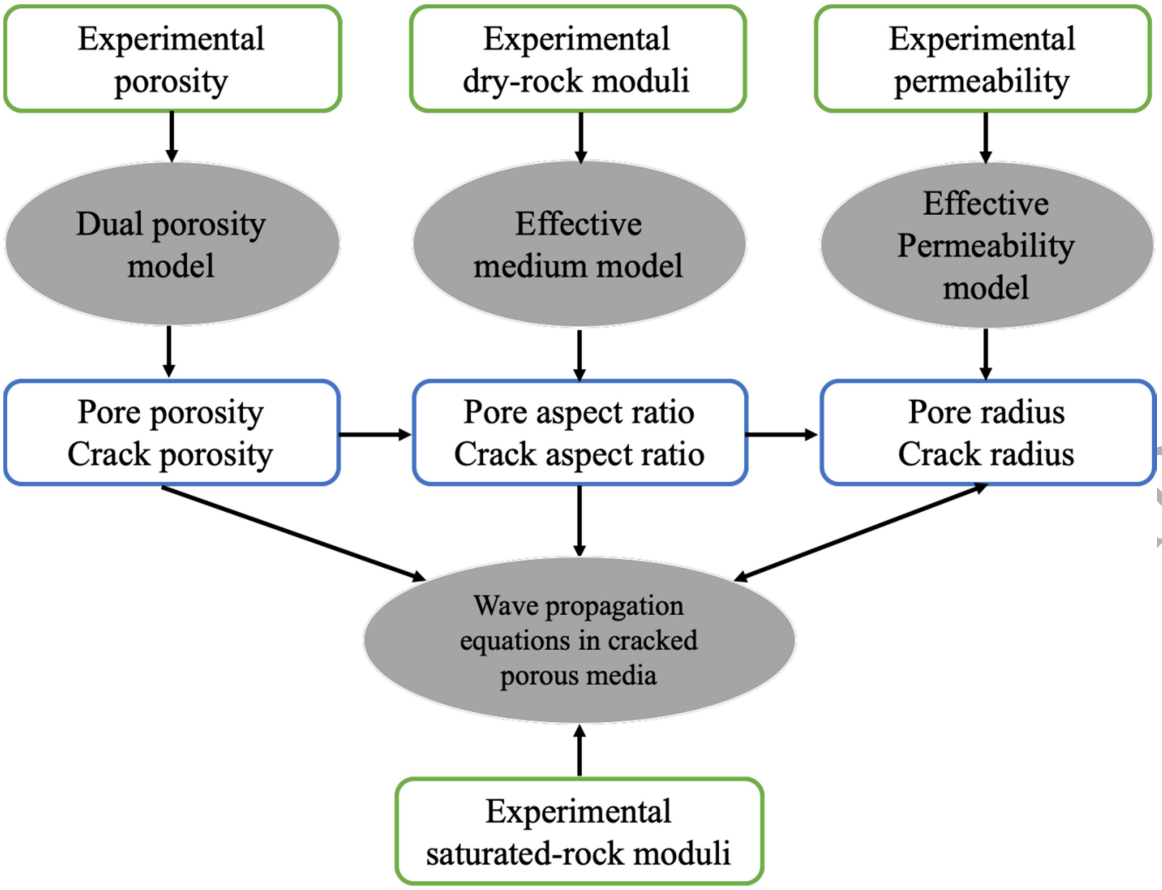

Figure 2. Workflow of the pore microstructure prediction based on experimental data and theoretical models

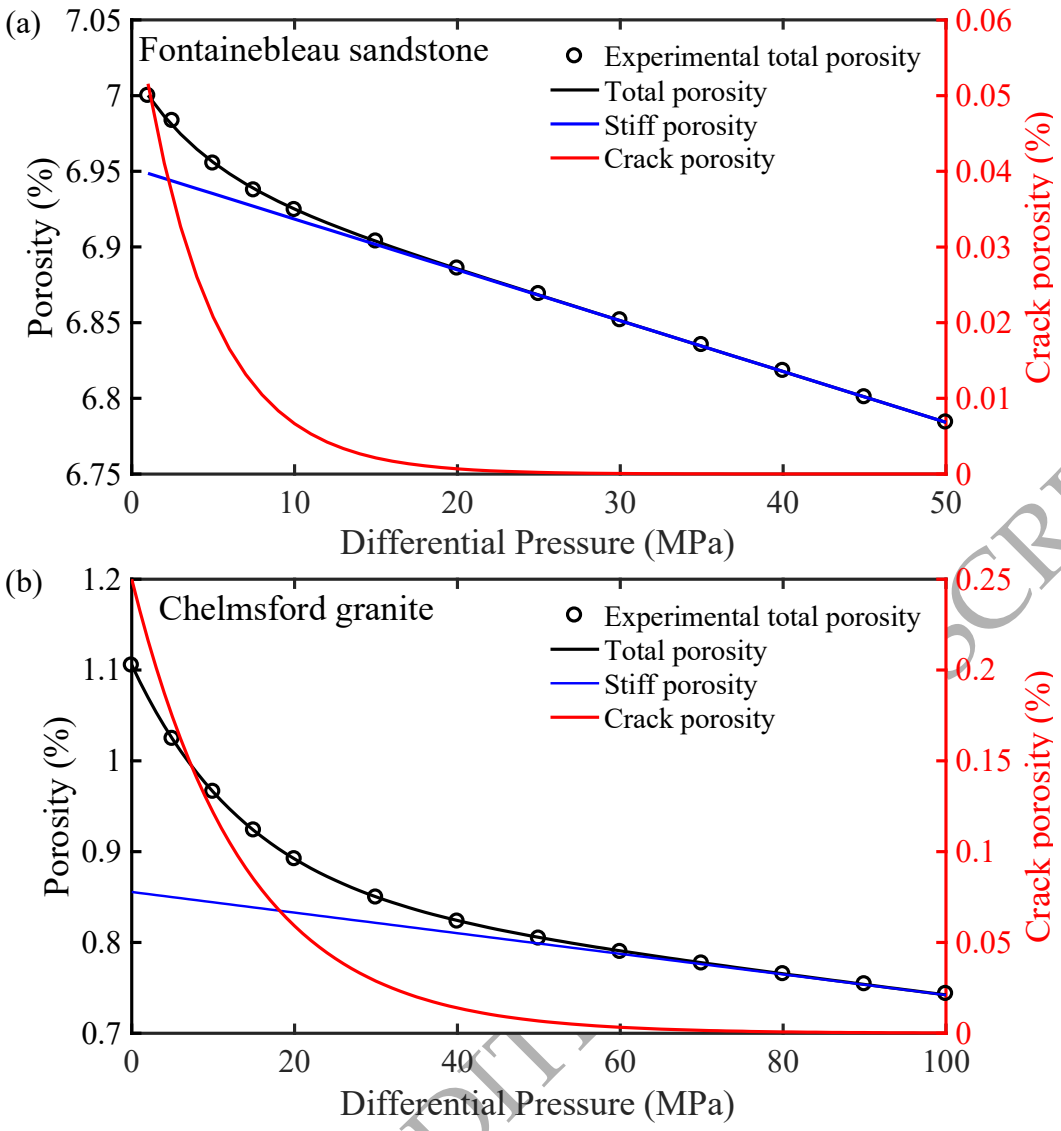

Figure 3. Total, stiff and crack porosities as a function of the differential pressure for Fontainebleau sandstone (a) and Chelmsford granite (b). The black circles denote the experimental data, the solid black, blue and red lines refer to the total, stiff and crack porosities based on the dual-porosity model.

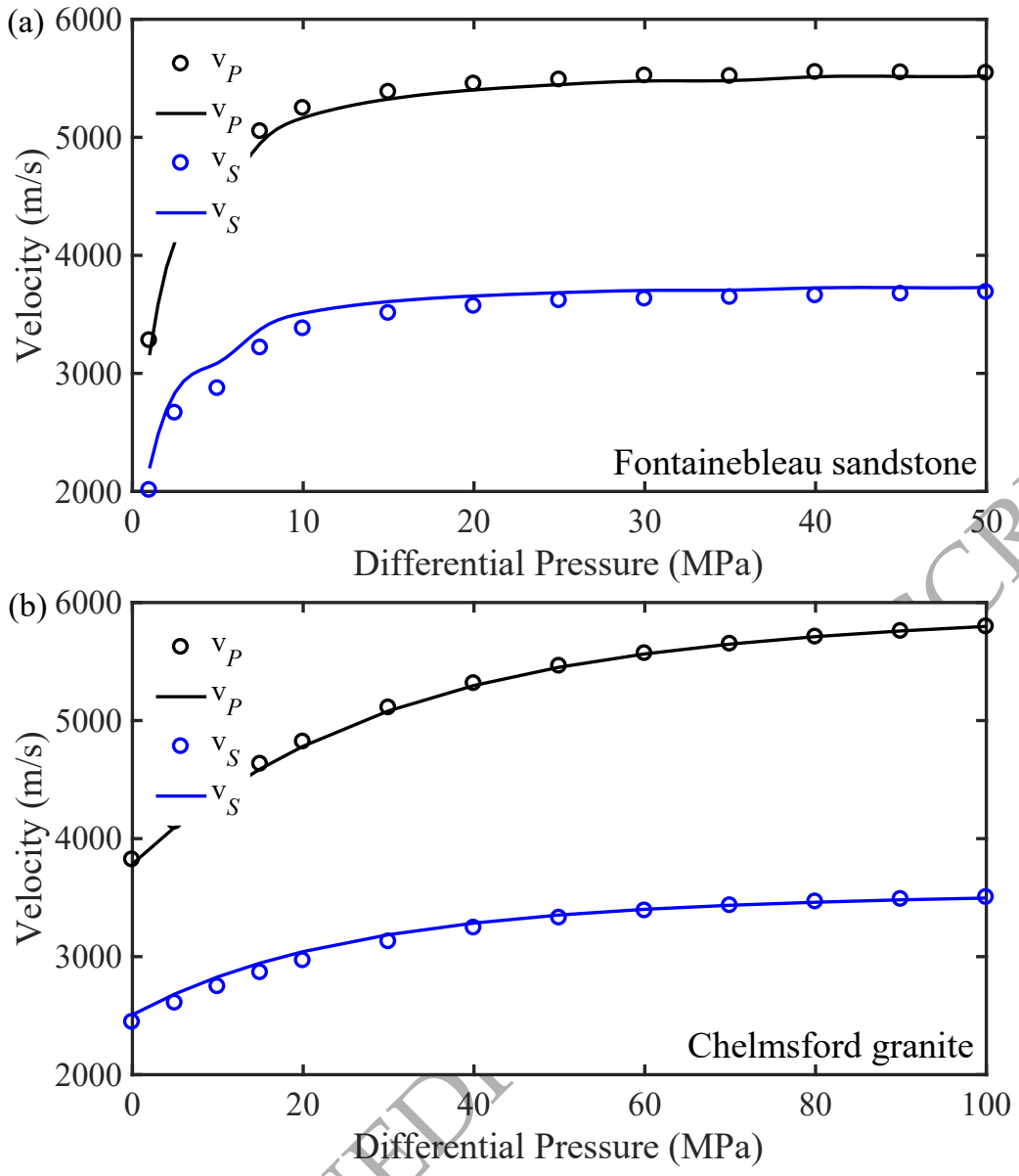

Figure 4. P- and S-wave velocities as a function of the differential pressure for Fontainebleau sandstone (a) and Chelmsford granite (b). The solid lines are the fit with the DEM model and the circles are measurements.

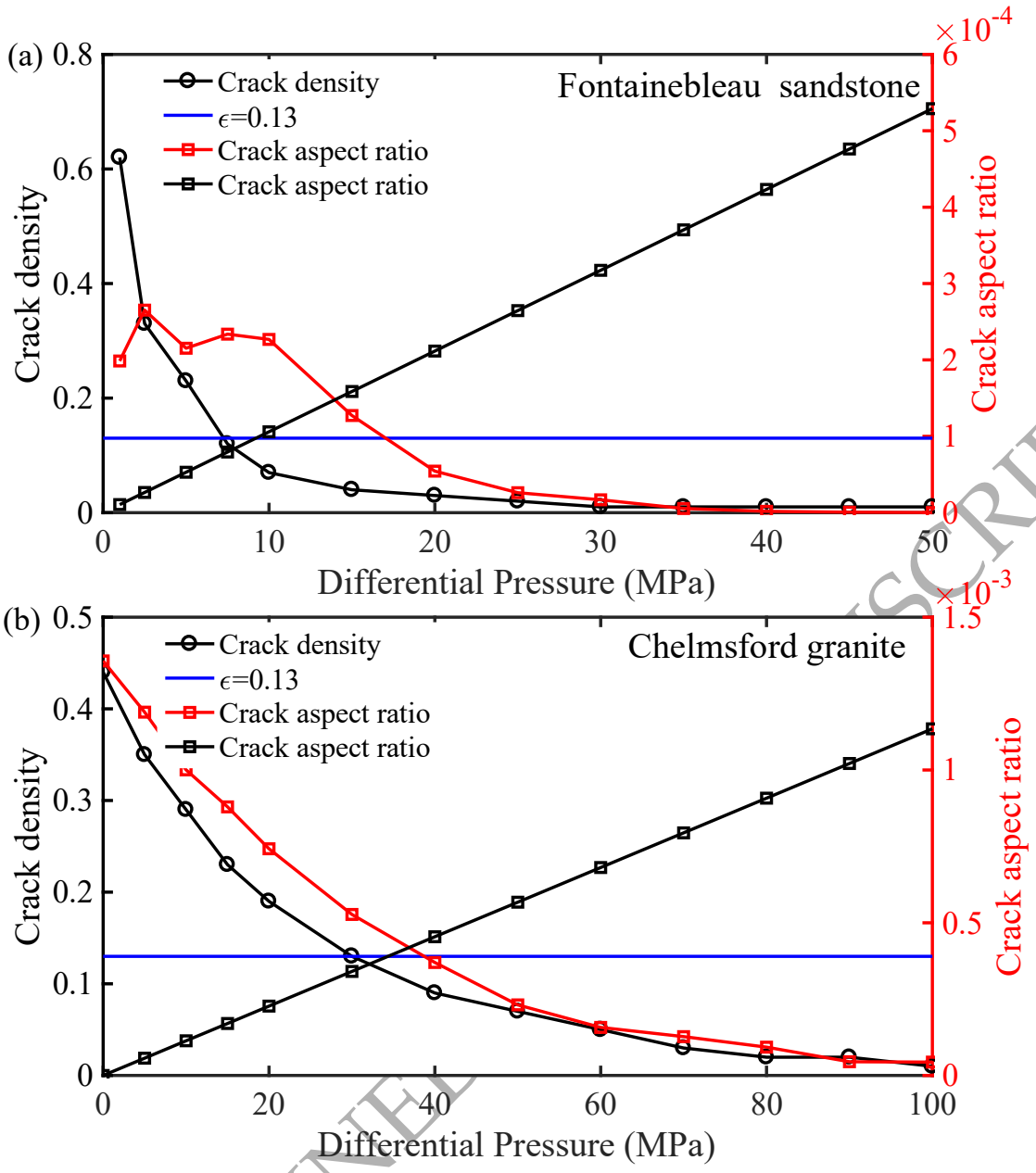

Figure 5. Crack densities and aspect ratio as a function of the differential pressure for Fontainebleau sandstone (a) and Chelmsford granite (b). The solid black line with circles denotes the crack density, the solid red line with squares are the crack aspect ratio, the solid black line with squares are the crack aspect ratio from $P_c \sim E\gamma$ and the solid blue line respresnets the corresponding crack density at ε =0.13.

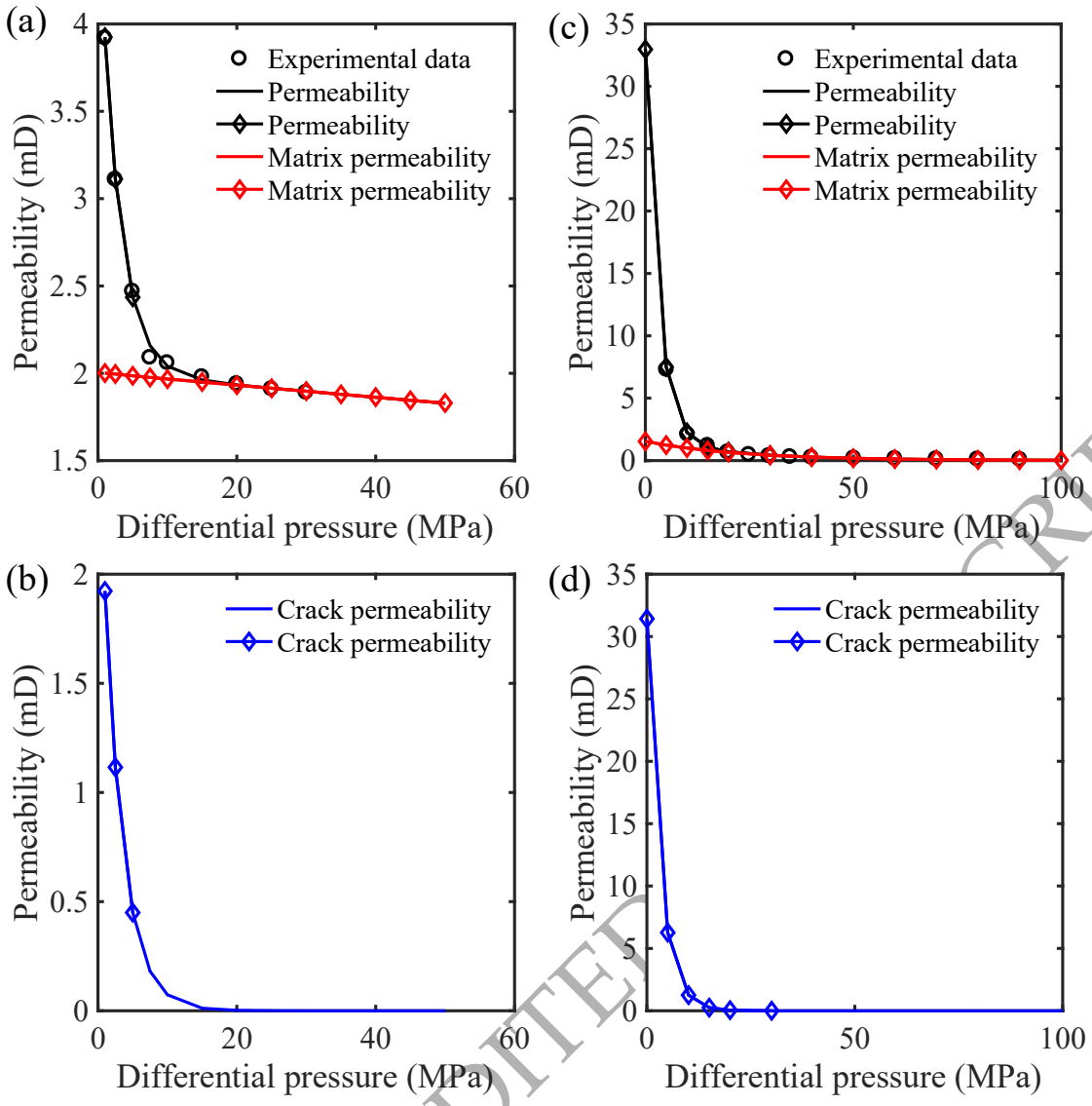

Figure 6. Total, matrix and crack permeability as a function of the differential pressure for Fontainebleau sandstone (a,b) and Chelmsford granite (c,d). The black circles denote the experimental data; the solid black, red and blue lines refer to the total, matrix and crack permeabilities from equation (8), respectively; the solid black, red and blue lines with diamonds refer the to the total, matrix and crack permeabilities from equations (9) and (10).

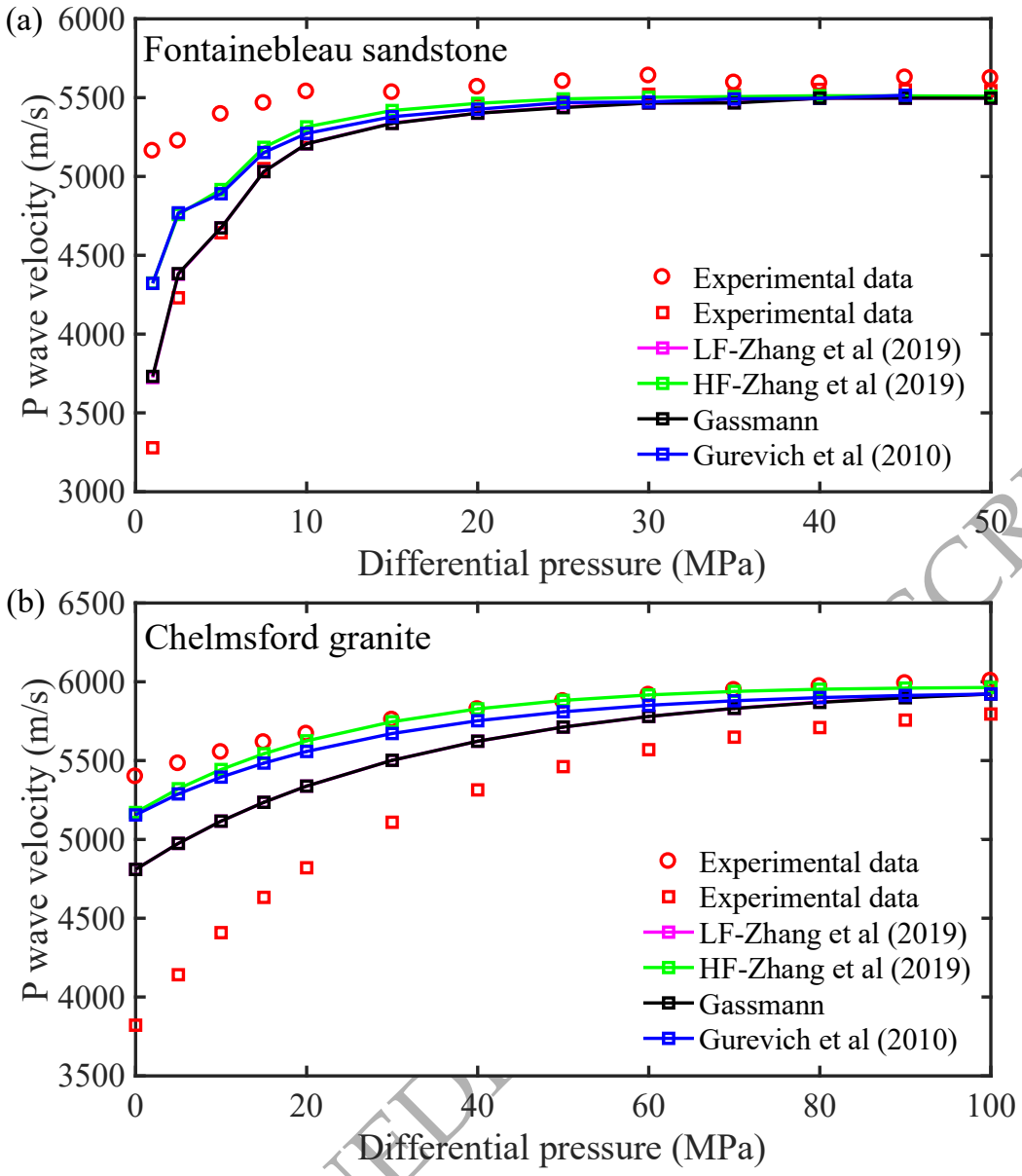

Figure 7. Comparison of the experimental and theoretical P-wave velocities for saturated Fontainebleau sandstone (a) and Chelmsford granite (b). The red circles and squares denote the experimental data at saturated and dry conditions, the solid pink and green lines with squares indicate the modeling results at low and high frequencies by using the equation (11), the solid black line with squares refer to the modeling results at low frequencies by using Gassmann equation (Gassmann 1951), and the solid blue line with squares to the theory at high frequencies (Gurevich et al., 2010).

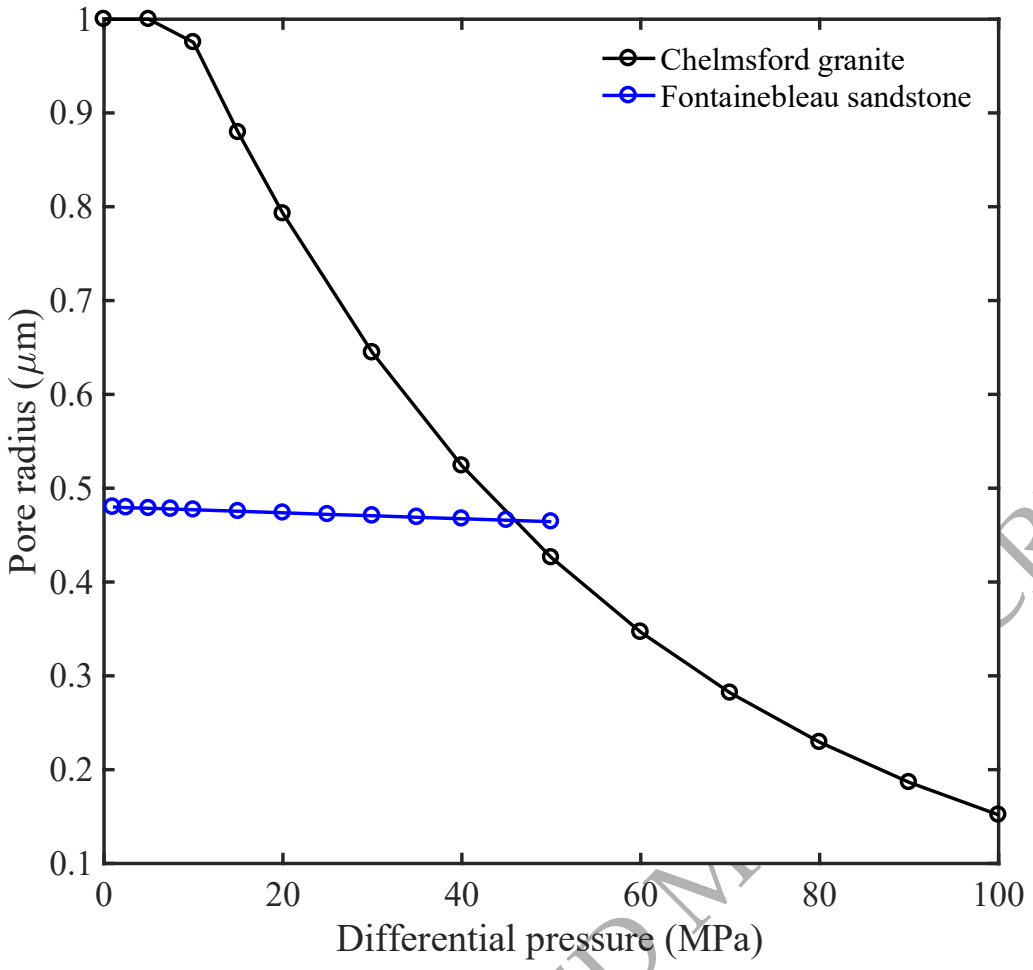

Figure 8. Pore radius as a function of the differential pressure. The solid blue line with circles corresponds to Fontainebleau sandstone, and the solid black line with circles denotes to Chelmsford granite.

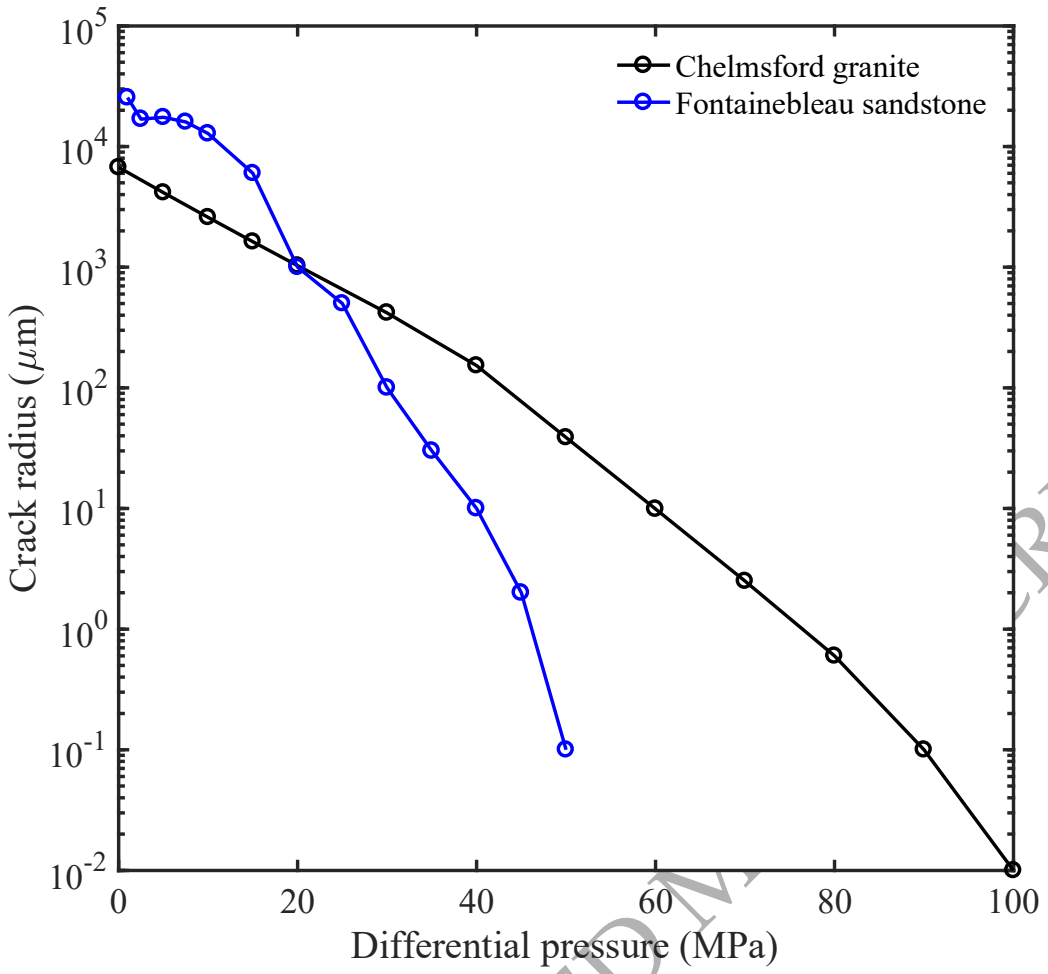

Figure 9. Crack radius as a function of the differential pressure. The solid blue line with circles corresponds to Fontainebleau sandstone, and the solid black line with circles denotes to Chelmsford granite.

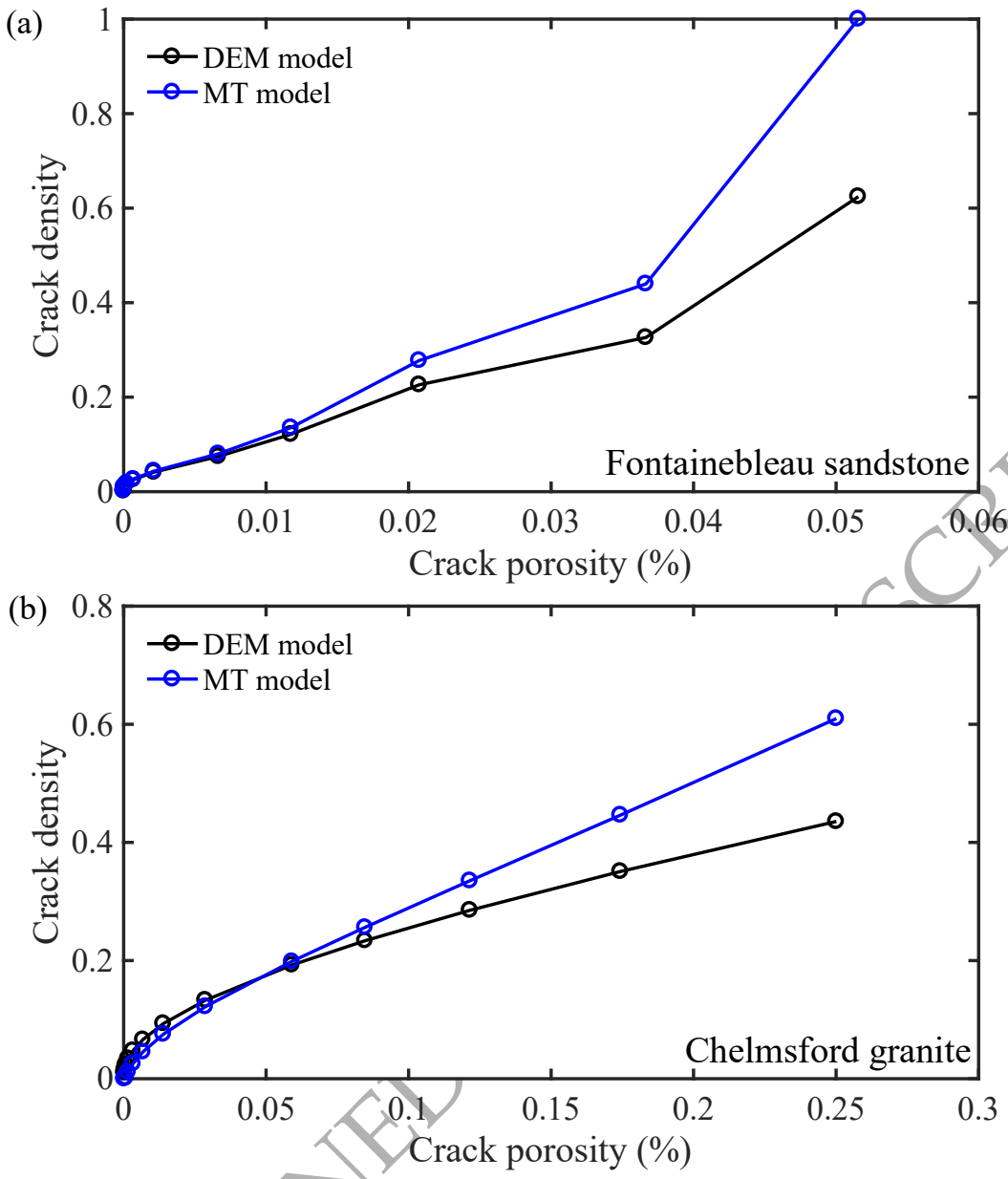

Figure 10. Crack density as a function of the crack porosity. The solid blue line with circles refers to the predictions of the MT model, and the solid black line with circles refers to predictions of the DEM model.